Supplemental Material

Higher-Order Weyl Semimetals

Hai-Xiao Wang,[1, 2, 3, 4], Zhi-Kang Lin,[1] Bin Jiang, [1] Guang-Yu Guo,[3, 4] and Jian-Hua Jiang[1,*]

[1]*School of Physical Science and Technology, & Collaborative Innovation Center of Suzhou Nano Science and Technology, Soochow University, 1 Shizi Street, Suzhou 215006, China*
[2]*School of Physical Science and Technology, Guangxi Normal University, Guilin 541004, China*
[3]*Department of Physics and Center for Theoretical Sciences, National Taiwan University, Taipei 10617, Taiwan*
[4]*Physics Division, National Center for Theoretical Sciences, Hsinchu 30013, Taiwan*

[*]Corresponding author： jianhuajiang@suda.edu.cn

I. Calculation of Wannier bands using the Wilson-loop approach

To study the Wannier bands and other properties of the model introduced in the main text, we transform the real-space tight-binding model into the wavevector-space form using the Fourier transformation, which yields the following tight-binding Hamiltonian,

$$H(\boldsymbol{k})$$
$$= \begin{bmatrix} 0 & \left(1+e^{-ik_z}\right)\left(t_1+t_2e^{-i(k_x+k_y)}\right) & \gamma+\lambda e^{-ik_x} & \gamma+\lambda e^{-ik_y} \\ & 0 & e^{ik_z}(\gamma+\lambda e^{ik_y}) & \gamma+\lambda e^{ik_x} \\ & h.c. & 0 & \left(1+e^{-ik_z}\right)\left(t_1+t_2e^{-i(-k_x+k_y)}\right) \\ & & & 0 \end{bmatrix}, (S1)$$

where $t_1=0.2, t_2=0.24, \gamma=0.5, \lambda=1$. The synthetic gauge fluxes introduced by the square-spiral structure play a key role on the emergence of the higher-order Weyl points, which act as transition points between the QAHI and HOTI phases. To visualize the process of topological transitions, we first present the band structure with various k_z in Fig. S1. A quadratic Weyl point appears at the Γ point with $k_z=0$ [see Fig. S1(a)]. Such a quadratic degeneracy between the 2nd and 3rd bands is lifted at increased k_z, which thus gives rise to a topological band gap with Chern number 1 (labeled by the light green region) [see Fig. S1(b)]. This process is equivalent to the synthetic gauge flux insertion which breaks the time-reversal symmetry and leads to quantum anomalous Hall effect, if we view the 3D system as many k_z-dependent 2D systems. At $k_z=0.473\pi$, the band gap closes at the M point indicates the emergence of the higher-order Weyl points [see Fig. S1(c)]. Further increase of k_z opens a band gap with quadrupole topology (indicated by the orange region) [see Fig.S1(d)]. We remark that the processes of band gap closing and reopening indicate the topological transitions between the QAHI and HOTI phases.

In the following, we characterize the QAHI and HOTI phases by computing the Chern number and the quadrupole index, respectively, using the Wilson-loop and nested Wilson-loop approaches. Our numerical approaches are applied to the first and second bands together, since the band gap of concern in this work is that between the second

and the third bands. Throughout this work, the HOTI phase refers to the quadrupole topological insulator (QTI) phase.
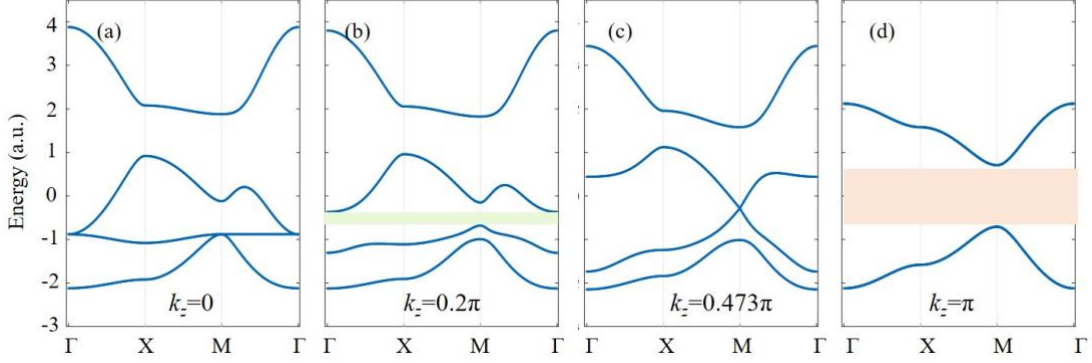

Fig. S1 The band structures for (a) $k_z = 0$, (b) $k_z = 0.2\pi$, (c) $k_z = 0.6\pi$, (d) $k_z = \pi$, showing the process of topological transitions. The light green (orange) region refers to band gaps with Chern number 1 (nontrivial quadrupole topology).

First, we utilize the Wilson-loop approach to calculate the Chern number, which is manifested as the winding number of the Wannier center in the reciprocal space. Specifically, the Brillouin zone is discretized into 200×200 k-points, of which k_x is split into an array k_{x1}, k_{x2}, ..., k_{xN} for each k_y, with $N = 201$. In the tight-binding model, the periodic part of the Bloch function $u_n(\mathbf{k}, \mathbf{r})$ are identical to the Bloch function $\psi_n(\mathbf{k}, \mathbf{r})$. Once all the $u_n(\mathbf{k}, \mathbf{r})$ are prepared, the Wilson-loop operators can be calculated directly. We first consider the Wilson-loop operators for the loops along the x direction, denoted as $\mathcal{W}_{x,\mathbf{k}}$, where $\mathbf{k} = (k_x, k_y)$ is the starting point of the loop. Using the discretized Berry connection matrix $[F_{x,\mathbf{k}}]^{mn} = <u_{m,\mathbf{k}}|u_{n,\mathbf{k}+\Delta k_x}>$ with $\Delta k_x = \frac{2\pi}{N-1}$, $m, n = 1,2$, the Wilson-loop operator (matrix) is computed as $\mathcal{W}_{x,\mathbf{k}} = \prod_{i=0}^{N-1} F_{x,\mathbf{k}+i\Delta k_x}$. We then diagonalize the Wilson-loop operator $\mathcal{W}_{x,\mathbf{k}}|v_{x,\mathbf{k}}^j> = e^{i2\pi v_x^j(k_y)}|v_{x,\mathbf{k}}^j>$, where $j = 1,2$ is the Wannier band index, and $|v_{x,\mathbf{k}}^j>$ is the eigenvector which depends on both the direction and the starting point of the Wilson-loop. The phase v_x^j gives the Wannier centers of the first and second

Bloch bands. As k_y goes from k_{y1} to k_{yN}, the evolution of v_x^j forms the Wannier

bands. The Wilson-loop operators in the y direction $\mathcal{W}_{y,\mathbf{k}}$ and its eigenvalues can be

computed similarly, yielding the Wannier bands denoted as $v_y^j(k_x)$.

In Fig. S2, we present the Wannier bands $v_y^j(k_x)$ $[v_x^j(k_y)]$ ($j = 1,2$, refers to the

band index) for $k_z = 0.2\pi$ and $k_z = \pi$. The gapless Wannier band is made up of two

eigenvalues of the Wilson-loop operator, indicating the non-zero Chern number of the

first and second bands. The Chern number is given by the winding number of the

Wannier bands $v_y(v_x)$ [1]. From Fig. S2, the Chern number of the first and the second
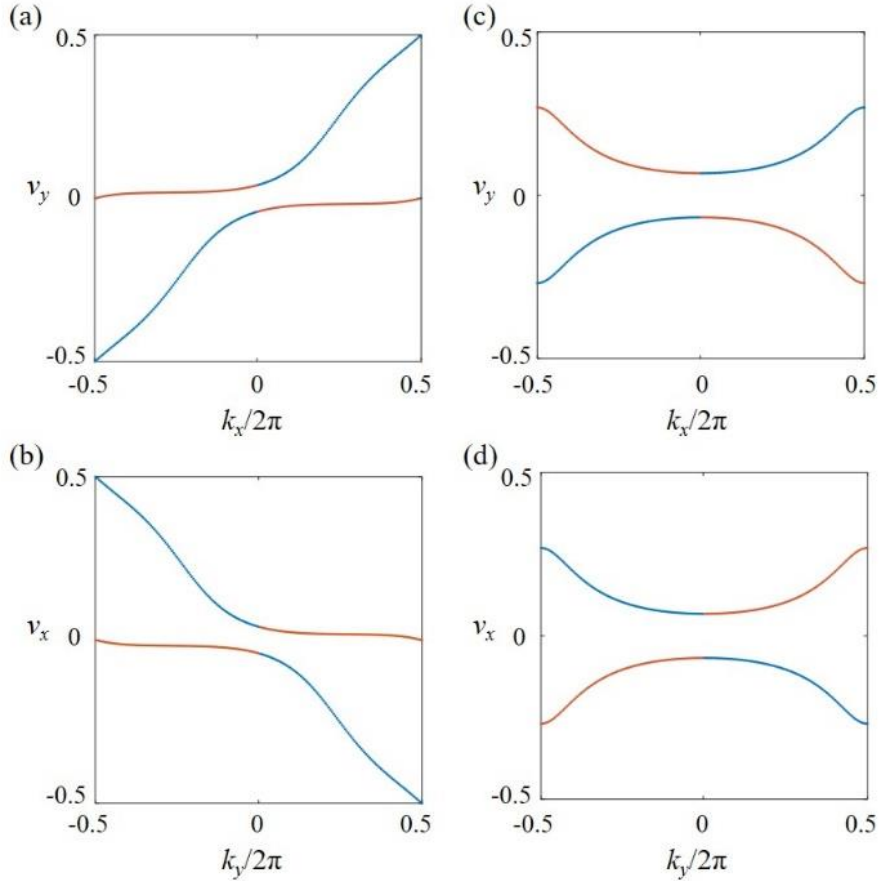
bands together is -1.

Fig. S2 The Wannier band for (a,c) $k_z = 0.2\pi$, (c,d) $k_z = \pi$. The winding number of the
Wannier center in (a,c) gives the Chern number -1. The gapped Wannier band in (b,d) indicates
offers the possibility to calculate the polarization of the Wannier bands.

In comparison, the Wannier bands for the lowest two energy bands at $k_z = \pi$ are gapped, as one signature of the quadrupole topology. Moreover, the results show that the Wannier bands $v_y(v_x)$ as a function of $k_x(k_y)$ always sum up to 0, proving that the bulk dipole is zero, i.e., $p_x = p_y = 0$ (a necessary condition for the quadrupole topology). We remark that the Wannier bands have the following symmetry, $\{v_x^j(k_y)\} = \{-v_x^j(-k_y)\} \, mod \, 1$, which is the consequence of the symmetry constraints due to the S_x, S_y and the time-reversal symmetries. The proof of the symmetry constraints on the Wannier bands are provided in Sec.III.

II. Calculation of the quadrupole index

We now calculate the quadrupole index for $|k_z| > 0.473\pi$ to characterize the HOTI phase. Taking $k_z = \pi$ as an example, the gapped Wannier bands provide the necessary condition for the definition and calculation of the nested Wannier bands through which the quadrupole index is computed. The Wannier bands are split into two sectors [see Fig. S2 (c,d)]: the positive and negative sectors, labeled by the superscripts $\pm$, respectively. The corresponding Wannier band wavefunctions are given by [1] $|w_{x,\mathbf{k}}^{\pm}\rangle = \sum_n |u_{\mathbf{k}}^n\rangle [v_{x,\mathbf{k}}^{\pm}]^n$. The key feature is that, being gapped, the Wannier bands can carry their own topological invariant which is the Wannier band polarizations. The discretized Berry connection for the Wannier band wavefunctions is given by [1] $F_{y,\mathbf{k}}^{\pm} = <w_{x,\mathbf{k}}^{\pm}|w_{x,\mathbf{k}+\Delta k_y}^{\pm}>$ with $\Delta k_y = \frac{2\pi}{N-1}$. The nested Wilson-loops along the k_y direction are obtained as $\widetilde{\mathcal{W}}_{y,\mathbf{k}}^{\pm} = \prod_{i=0}^{N-1} F_{y,\mathbf{k}+i\Delta k_y}^{\pm}$. We then diagonalize the nested Wilson-loop operator which gives the eigenvalues $e^{i2\pi p_y^{v_x^{\pm}}(k_x)}$. These eigenvalues give the nested Wannier bands $p_y^{v_x^{\pm}}(k_x)$ [1]. The nested Wilson-loops along the k_x direction $\widetilde{\mathcal{W}}_{x,\mathbf{k}}^{\pm}$ can be computed similarly, yielding the nested Wannier bands $p_x^{v_y^{\pm}}(k_y)$. The Wannier band polarizations are given by the average of the nested Wannier bands as follows [1]: $P_x^{v_y^{\pm}} = \frac{1}{2\pi}\int d\, k_y p_x^{v_y^{\pm}}(k_y)$ and $P_y^{v_x^{\pm}} = \frac{1}{2\pi}\int d\, k_x p_y^{v_x^{\pm}}(k_x)$.

We numerically compute the Wannier band polarizations and find that $P_x^{v_{\bar{y}}} = P_y^{v_{\bar{x}}} = \frac{1}{2}$ (see Fig. S3). Therefore, the $k_z = \pi$ case have a nontrivial quadrupole index of $q_{xy} = 2P_x^{v_{\bar{y}}} P_y^{v_{\bar{x}}} = \frac{1}{2}$.
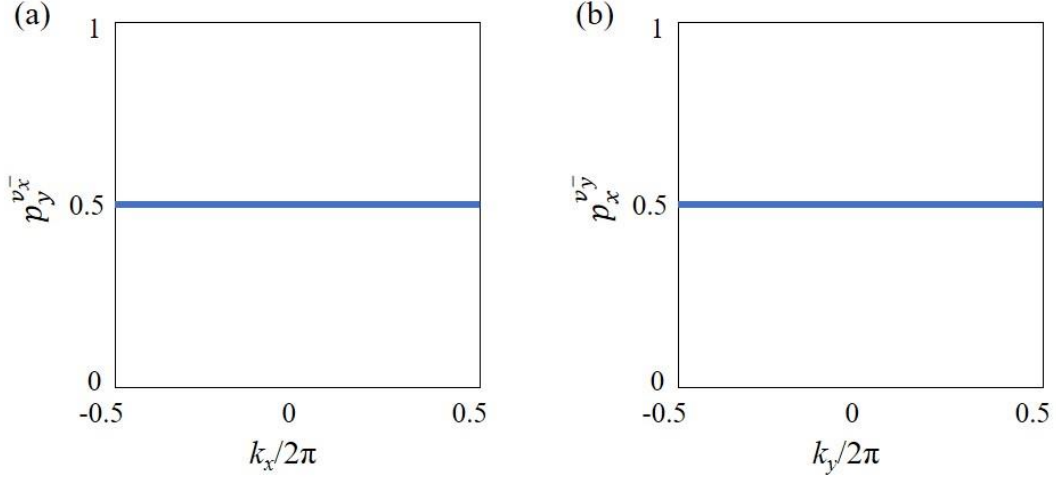

Fig. S3 Calculation of the nested Wannier bands (a) $p_y^{v_{\bar{x}}}(k_x)$ and (b) $p_x^{v_{\bar{y}}}(k_y)$ for $k_z = \pi$, showing that the quadrupole index is nontrivial and is quantized to $\frac{1}{2}$.

III. Symmetry constraints and the quantization of Wannier band polarizations

In this section, we focus on the constraints imposed by the rotation symmetries on the Wannier bands and the nested Wannier bands. Following Ref. [1], the constraints of a symmetry operator D_g over the Wilson-loop $\mathcal{W}_{C,\mathbf{k}}$ satisfies the following relation

$$B_{g,\mathbf{k}} \mathcal{W}_{C,\mathbf{k}} B_{g,\mathbf{k}}^\dagger = \mathcal{W}_{D_g C, D_g \mathbf{k}}, \qquad (S2)$$

where the first subscript C in the Wilson-loop operator $\mathcal{W}_{C,\mathbf{k}}$ refers to the contour loop, and the second subscript $\mathbf{k}$ is the starting point of the Wilson-loop. $B_{D_g \mathbf{k}}^{mn} = < u_{D_g \mathbf{k}}^m | g_\mathbf{k} | u_\mathbf{k}^n >$ is the unitary matrix that connects the Bloch states at $\mathbf{k}$ with those at $D_g \mathbf{k}$, which have the same energy, $g_\mathbf{k}$ is the unitary operator in the Bloch-Hilbert space corresponding to the symmetry operator D_g in the wavevector space, which transforms the Hamiltonian $h_\mathbf{k}$ as follows

$$g_{\mathbf{k}} h_{\mathbf{k}} g_{\mathbf{k}}^{-1} = h_{D_g \mathbf{k}}. \tag{S3}$$

We define the Wilson-loops along the contour $\mathcal{C}_1 = (k_x, k_y) \to (k_x + 2\pi, k_y)$ with increasing (decreasing) k_x as $\mathcal{W}_{\mathcal{C}_1, \mathbf{k}}$ ($\mathcal{W}_{\mathcal{C}_1, -\mathbf{k}}$) and $\mathcal{C}_2 = (k_x, k_y) \to (k_x, k_y + 2\pi)$ with increasing (decreasing) k_y as $\mathcal{W}_{\mathcal{C}_2, \mathbf{k}}$ ($\mathcal{W}_{\mathcal{C}_2, -\mathbf{k}}$), where $\mathbf{k} = (k_x, k_y)$ is the starting point of the Wilson-loop.

a. Constraints on the Wannier bands due to Θ_y

First of all, let us introduce the anti-unitary operator $\Theta_y = S_{2y} T$, where $S_{2y}: (x, y, z) \to (-x, y, -z - \frac{1}{2})$ and T is the time-reversal operator. Note that $\Theta_y \mathbf{k} = S_{2y} T(k_x, k_y, k_z) = (k_x, -k_y, k_z)$. Therefore, in the wavevector space, the Θ_y is equivalent to that of the mirror reflection $M_y: (x, y, z) \to (x, -y, z)$ studied in Ref. [1] to derive the constraints on the (nested) Wannier bands imposed by the reflection symmetries. Considering the symmetry constraints on the Wilson-loop operator along the contour $\mathcal{C}_1$, we have

$$B_{\Theta_y, \mathbf{k}} \mathcal{W}_{x, \mathbf{k}} B_{\Theta_y, \mathbf{k}}^{\dagger} = \mathcal{W}_{-x, M_y \mathbf{k}} = \mathcal{W}_{x, M_y \mathbf{k}}^{\dagger}, \tag{S4}$$

where $B_{\Theta_y, \mathbf{k}}^{mn} = <u_{\Theta_y \mathbf{k}}^m | g_{\mathbf{k}} | u_{\mathbf{k}}^n>$ is the unitary sewing matrix that connects the Bloch states at $\mathbf{k}$ with those at $\Theta_y \mathbf{k}$. The $g_{\mathbf{k}}$ is the unitary matrix operator. Thus, the Wilson-loop at $\mathbf{k}$ is equivalent (up to a unitary transformation) to the Hermitian conjugate of the Wilson-loop at $M_y \mathbf{k}$. Since the eigenvalues of the Wilson-loop operator are independent, this directly yields,

$$\left\{ e^{i2\pi v_x^j(k_y)} \right\} = \left\{ e^{-i2\pi v_x^{j'}(-k_y)} \right\}, \tag{S5a}$$

or equivalently

$$\left\{ v_x^j(k_y) \right\} = \left\{ -v_x^{j'}(-k_y) \right\} \bmod 1. \tag{S5b}$$

Obviously, $j' = -j$ where $j = \pm$ labels the Wannier sectors. In the above equations, $\{...\}$ implies the set of eigenvalues. On the other hand, by considering the symmetry

constraint on the Wilson-loop along the contour C_2, we find that such a symmetry implies the following trivial constraint

$$\{v_y^j(k_x)\} = \{v_y^j(k_x)\} \ mod \ 1. \tag{S6}$$

b. Constraints on the Wannier bands due to Θ_x

In parallel, we construct another anti-unitary operator $\Theta_x = S_{2x}T$, where $S_{2x}: (x, y, z) \to (x, -y, -z)$ and T is the time-reversal operator. In the wavevector space, the symmetry operator Θ_x transforms (k_x, k_y, k_z) to $(-k_x, k_y, k_z)$, which is equivalent to that of the mirror reflection $M_x: (x, y, z) \to (-x, y, z)$. By considering the symmetry constraint on the Wilson-loop along the contour C_2 in Eq.($S2$) for the symmetry operator Θ_x, we have

$$B_{\Theta_x,\mathbf{k}}\mathcal{W}_{y,\mathbf{k}}B_{\Theta_x,\mathbf{k}}^{\dagger} = \mathcal{W}_{-y,M_x\mathbf{k}} = \mathcal{W}_{y,M_x\mathbf{k}}^{\dagger}. \tag{S7}$$

Following the above procedure and analysis, one has

$$\left\{e^{i2\pi v_y^j(k_x)}\right\} = \left\{e^{-i2\pi v_y^{j'}(-k_x)}\right\}, \tag{S8a}$$

or equivalently

$$\{v_y^j(k_x)\} = \left\{-v_y^{j'}(-k_x)\right\} \ mod \ 1. \tag{S8b}$$

Obviously, $j' = -j$ where $j = \pm$ labels the Wannier sectors. On the other hand, by considering the symmetry constraint on the Wilson-loop along the contour C_1, we find that such a symmetry implies the following trivial constraint

$$\{v_x^j(k_y)\} = \{v_x^j(k_y)\} \ mod \ 1. \tag{S9}$$

c. Constraints on the nested Wannier bands due to Θ_y

Using Eq. ($S5b$) and keeping in mind that in the reciprocal space $\Theta_y\mathbf{k} = S_{2y}T(k_x, k_y, k_z) = (k_x, -k_y, k_z)$, intuitively, the invariance of the nested Wilson-loops under the symmetry operator Θ_x is expressed as

$$\left\{ e^{i2\pi p_y^{v_x^j}(k_x)} \right\} = \left\{ e^{-i2\pi p_y^{v_x^j}(-k_x)} \right\}, \tag{S10a}$$

or equivalently

$$\left\{ p_y^{v_x^j}(k_x) \right\} = \left\{ -p_y^{v_x^j}(-k_x) \right\} \ mod \ 1, \tag{S10b}$$

where $j = \pm$ labels the Wannier sectors. The Wannier band polarizations can be written as

$$P_y^{v_x^j} = \frac{1}{N_{k_x}} \sum_{k_x} p_y^{v_x^j}(k_x) \ mod \ 1. \tag{S11}$$

Since k_x is a dummy variable (N_{k_x} is the total number of k_x), the symmetry invariance associated with Θ_y implies that

$$P_y^{v_x^j} = -P_y^{v_x^j} \ mod \ 1. \tag{S12}$$

d. Constraints on the nested Wannier bands due to Θ_x

In parallel, the invariance of the nested Wilson-loops under the Θ_x is written as

$$\left\{ e^{i2\pi p_x^{v_y^j}(k_y)} \right\} = \left\{ e^{-i2\pi p_x^{v_y^j}(-k_y)} \right\}, \tag{S13a}$$

or equivalently

$$\left\{ p_x^{v_y^j}(k_y) \right\} = \left\{ -p_x^{v_y^j}(-k_y) \right\} \ mod \ 1, \tag{S13b}$$

where $j = \pm$ labels the Wannier sectors. The Wannier band polarizations can be written as

$$P_x^{v_y^j} = \frac{1}{N_y} \sum_{k_y} p_x^{v_y^j}(k_y) \ mod \ 1. \tag{S14}$$

Since k_y is a dummy variable, the symmetry Θ_x implies that

$$P_x^{v_y^j} = -P_x^{v_y^j} \bmod 1. \tag{S15}$$

d. Quantization of the quadrupole index

Summarizing the above constraints, we find that

$$P_x^{v_y^j} = 0, \frac{1}{2} \bmod 1, \tag{S16}$$

for both Wannier sectors v_y^+ and v_y^-. Since the x and y directions are identical for the system with fourfold screw symmetry S_{4z} , we have

$$P_x^{v_y^j} = P_y^{v_x^j} = 0, \frac{1}{2} \bmod 1. \tag{S17}$$

With such quantizations of the Wannier band polarizations, the quantization of the quadrupole index is deduced as [1],

$$q_{xy} = 2P_x^{v_y^-} P_y^{v_x^-} = 0, \frac{1}{2} \bmod 1. \tag{S18}$$

Therefore, the quadrupole index is quantized by the symmetries Θ_x and Θ_y.

IV. Calculation of the fractional hinge charge

In this section, we present the details of the fractional hinge charge calculation. To calculate the hinge charge, we first consider a hinge region with 4×4 unit-cells areas in a finite system with 20×20 unit-cells in the x-y plane, because the wavefunction is not well localized at the hinges. According to the definition of the hinge charge, i.e., $Q_h = \sum_\alpha P_\alpha^{hinge} \bmod 1$, only the filled bulk states α are taken into account. Note that occupied localized hinge states only contribute an integer charge to Q_h, hence their contributions can be ignored. P_α^{hinge} is the probability of finding an electron in the hinge region for a occupied bulk states α (i.e., the bulk states in the first and second bulk bands). It should be noted that the hinge charge calculation is valid only for the insulator phases on the left and right sides of the higher-order Weyl points. The results are shown in Fig. 4(c) in the main text.

V. Details of the surface and hinge LDOS calculations

In this work, the surface LDOS is calculated from the eigenstates and spectrum of a supercell illustrated in Figure S4a. The supercell is periodic in the y and z directions, but finite in the x direction. Normally, we take 20 unit-cells along the x direction in our calculations. The surface LDOS can be obtained from the following equation,

$$DOS^S(E) = \sum_i \frac{S_i}{\pi[(E - E_i)^2 + \Gamma^2]} \Gamma. \tag{19}$$

Here, E_i is the eigen-energy of the i-th eigen-states, E represents the energy at which the LDOS is measured. In our calculation, we set $\Gamma = 1/200$ for a good resolution in the figures. S_i denotes the probability of finding an electron in the surface region when the electron is in the eigenstate i. This probability is calculated from the wavefunction of the eigenstate. In the calculation of the results in Figure 3 in the main text, the surface region is chosen to be the leftmost unit-cell in the supercell illustrated in Figure S4a. Therefore, Figure 3 in the main text presents the surface LDOS only at one surface, for the demonstration of the chiral Fermi-arc surface states.

To calculate the hinge LDOS, we study a square supercell which is schematically illustrated in Fig. S4b. In our calculation, we numerically compute the eigenstates and spectrum of a square supercell with 20×20 unit-cells. The supercell is periodic along the z direction, but finite in the x and y directions. The hinge LDOS is calculated using the following equation,

$$DOS^H(E) = \sum_i \frac{H_i}{\pi[(E - E_i)^2 + \Gamma^2]} \Gamma, \tag{20}$$

where H_i represents the probability of finding an electron in the hinge regions when the electron is in the eigenstate i. The probability H_i is calculated from the wavefunction of the eigenstate i. Again, we set $\Gamma = 1/200$ for the sake of graphic presentation. In the calculation of the hinge LDOS, each hinge region includes 2×2 unit-cells. This is because the wavefunctions of the hinge states are not well-localized for the parameters considered in this work.
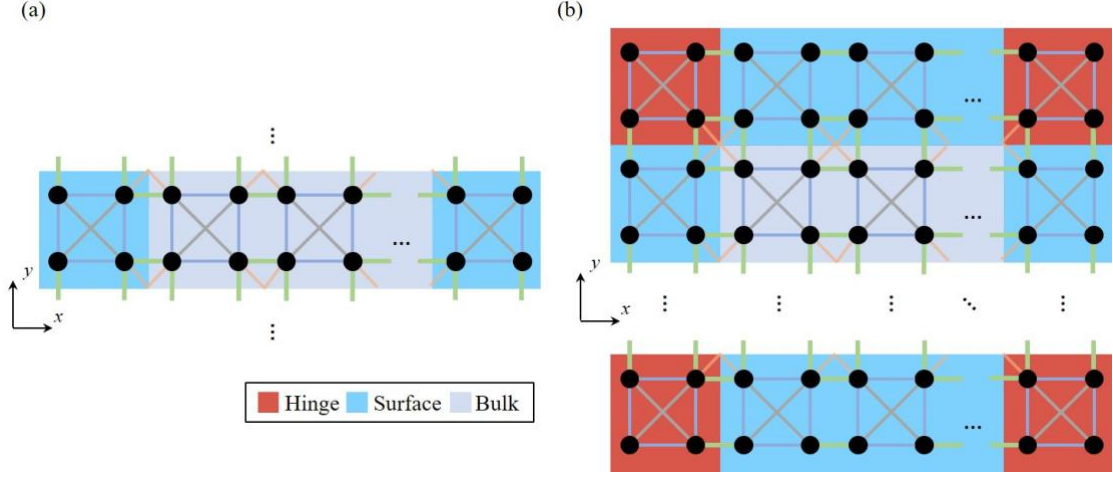
Figure S4 (a) Schematic illustration of the supercell for the calculation of the surface LDOS. (b) Schematic illustration of the supercell for the calculation of the hinge LDOS. The dots and lines denote, respectively, the lattice sites and the tight-binding couplings. Note that, in (b), for the sake of graphic representation, only one unit-cell is illustrated in each hinge (red) region. However, in our calculations, 2×2 unit-cells are included in each hinge region, because the hinge states are not well localized.

VI. Potential material candidates in acoustic and electronic systems

The predicted HOWPs can emerge in acoustic, electronic and photonic systems with the tetragonal crystalline symmetries presented in the main text. In this section, we suggest several possible materials that may realize the HOWPs.

First, we propose to realize the HOWPs using sonic crystals (SCs). Our design is illustrated in Fig. S5a where a SC made of layer-stacked acoustic resonators exhibiting the required fourfold screw symmetry S_{4z} and the twofold rotation symmetries C_{2x}, C_{2y}. The interlayer couplings are realized by air holes at the center and the corners of the unit-cell. The lattice constant in the x-y plane is $a = 20$ mm. In the z direction, the lattice constant is $H = 4(h_1 + h_2)$, where $h_1 = 0.2a$ and $h_2 = 0.1a$ are the heights depicted in Fig. S5a. The radii of the holes are $r_1 = 0.08a$, $r_1 = 0.17a$. The distance l is $0.25a$, while the thickness d is $0.1a$. Such a SC can be fabricated using the commercial 3D printing technology based on epoxy materials. In Fig. S5c1-

c4, we present the calculated band structures along the high symmetry lines for different k_z. It is evident that the second band gap experience a process of opening, closing and reopening, which indicates the topological phase transitions.
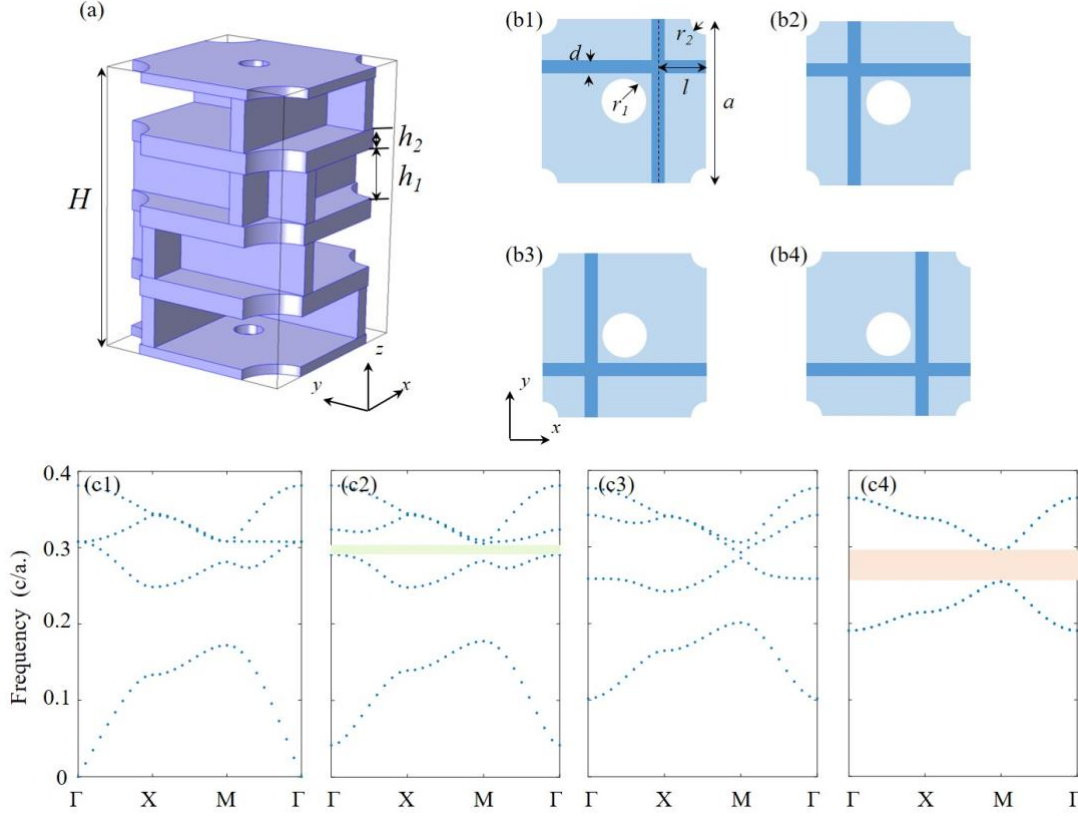

Fig. S5 A possible scheme to realize HOWPs in acoustic systems. (a) Schematic of the spiral sonic crystal. Darkblue regions are made of epoxy which can be regarded as hard-wall boundaries for the sound waves. (b1-b4) The top view of (b1) the 1st layer, (b2) the 2nd layer, (b3) the 3rd layer, (b4) the 4th layer where the darkblue regions represent the epoxy walls that separate the resonators in the same layer. (c1-c4) The band structure at (c1) $k_z = 0$, (c2) $k_z = 0.2\pi$, (c3) $k_z = 0.8\pi$, and (c4) $k_z = \pi$. The light green region refers to the band gap with a Chern number 1, while the orange region refers to the band gap with nontrivial quadrupole topology.

Table I. The eigenvalues of $\tilde{C}_{4z}$ and $\tilde{C}_{2z}$ at the high symmetry point (HSPs)

HSPs	1st Band	2nd Band	3rd Band	4th Band

	$(0,0,\pi)$	1	i	$-i$	-1
$\tilde{C}_{4z}$	(π,π,π)	-1	$-i$	1	i
	$(0,0,0.2\pi)$	1	i	$-i$	-1
	$(\pi,\pi,0.2\pi)$	-1	1	$-i$	i
$\tilde{C}_{2z}$	$(0,0,0.2\pi)$	1	-1	-1	1
	$(\pi,0,0.2\pi)$	-1	1	-1	1

To obtain the topological indices, we study the eigenvalues of the pseudo-rotation operators $\tilde{C}_{4z} = e^{-ik_z/4}S_{4z}$ and $\tilde{C}_{2z} = e^{-ik_z/2}S_{2z}$ (where $S_{2z} := (x,y,z) \to (-x,-y,z+\frac{1}{2})$ is a twofold screw rotation) at the $\tilde{\Gamma} = (0,0,k_z)$ and $\tilde{M} = (\pi,\pi,k_z)$ points, as displayed in Table I. For $k_z = \pi$, the $\tilde{C}_{4z}$ eigenvalue r_4^- at $\tilde{\Gamma}(\tilde{M})$ point is $i(-i)$. We thus obtain the quadrupole index as $q_{xy} = \frac{1}{2}$ according to Eq. (2) in the main text. The Chern number C can also be deduced from the symmetry eigenvalues at the high-symmetry points. According to Ref. [1], one has $C = \left[M_1^{(4)}\right] + 2\left[M_2^{(4)}\right] + 3\left[M_3^{(4)}\right] + 2\left[X_1^{(2)}\right] \mod 4$,where $\left[\Pi_p^{(n)}\right] = \# \Pi_p^{(n)} - \# \Gamma_p^{(n)}$, $p = 1,2 \ldots, n$. Here, $\# \Pi_p^{(n)}$ is the number of the occupied bands with the eigenvalue $\Pi_p^{(n)} = e^{\frac{2\pi i(p-1)}{n}}$. By substituting the symmetry eigenvalues as listed in Table I, we find that $\left[M_1^{(4)}\right] = 0$, $\left[M_2^{(4)}\right] = -1$, $\left[M_3^{(4)}\right] = 1$, $\left[X_1^{(4)}\right] = 0$ for $k_z = 0.2\pi$. Therefore, the band gap at $k_z = 0.2\pi$ has a Chern number $C = 1$.

In electronic systems, the HOWPs can be found in tetragonal chiral crystals. We notice that a large number of tetragonal chiral crystals either already exist in nature or have been grown (see, e.g., [2,3]). For example, binary compound Mg_3Ru_2 was found to crystallize in a tetragonal chiral structure with space group $P4_132$ [4]. Ternary compound $(TaSe_4)_2I$ forms a quasi-one-dimensional tetragonal crystal with chiral space group $I422$ [5]. Interestingly, it was recently reported to be a Weyl semimetal [6]. A simpler candidate is binary compound $SrSi_2$, which crystalizes in a tetragonal structure with the same chiral space group as that of Mg_3Ru_2 [7]. Excitingly, this disilicide was

recently found to be a new type of Weyl semimetal with quadratic double Weyl fermions [8]. We will carry out systematic *ab initio* density functional theory calculations for candidate tetragonal chiral crystals in search for specific Weyl semimetals with the HOWPs. Since such *ab initio* calculations themselves constitute a grand project, we will present our findings in our future publications.

Finally, we remark that in experiments, the two kinds of topological boundary states, i.e., the Fermi-arc surface states and hinge states are spatially separated and hence are easy to distinguish. For instance, they can be revealed by the spectral properties on the surface and hinges. The local density of states (LDOS) on the surfaces away from the hinges are solely due to the Fermi-arc surface states. From the surface LDOS one can deduce the spectra of the surface states. On the other hand, the LDOS at the hinge boundaries have contributions from both the hinge states and Fermi-arc surface states. Nevertheless, these two contributions are well-separated in wavevector and energy spaces: the hinge states emerge at large $|k_z|$ where the surface states become gapped (in fact, the hinge states emerge in such a gap), while the Fermi-arc surface states appear at small $|k_z|$ where the surface states are gapless. With these knowledges, it is thus possible to distinguish these two kinds of topological boundary states.

References:

[1] W. A. Benalcazar, B. A. Bernevig, and T. L. Hughes, Phys. Rev. B **96**, 245115 (2017).

[2] Inorganic Crystal Structure Database (ICSD), (Fachinformationszentrum Karlsruhe, Karlsruhe, Germany, 2015).

[3] Bilbao Crystallographic Server, http://www.cryst.ehu.es.

[4] R. Pottgen, V. Hlukhyy, A. Baranov and Y. Grin, Crystal structure and chemical bonding of Mg3Ru2, Inorg. Chem. **47**, 6051 (2008).

[5] P. Gressier, A. Meerschaut, L. Guemas, J. Rouxel, and P. Monceau, J. Solid State Chem. **51**, 141 (1984).

[6] W. Shi, B. J. Wieder, H. L. Meyerheim, Y. Sun, Y. Zhang, Y. Li, L. Shen, Y. Qi, L. Yang, J. Jena, P. Werner, K. Koepernik, S. Parkin, Y. Chen, C. Felser, B. A. Bernevig

and Z. Wang, A charge-density-wave Weyl semimetal, arXiv: 1909.04037v2 (2020).

[7] G. E. Pringle, The structure of SrSi2: a Crystal of Class O (432), Acta Cryst. B **28**, 2326 (1972).

[8] S. M. Huang, S.-Y. Xu, I. Belopolski, C.-C. Lee, G. Chang, T.-R. Chang, B. Wang, N. Alidoust, G. Bian, M. Neupane, D. Sanchez, H. Zheng, H.-T. Jeng, A. Bansil, T. Neupert, H. Lin, and M. Z. Hasan, New type of Weyl semimetal with quadratic double Weyl fermions, Proc. Natl. Acad. Sci. **113**, 1180 (2016).